


Article

Computational Methods for Modelling and Optimization of Flow Control Devices

Alejandro Ballesteros-Coll ¹, Unai Fernandez-Gamiz ^{1,*} , Iñigo Aramendia ¹ , Ekaitz Zulueta ² and Jose Manuel Lopez-Guede ² 

¹ Department of Nuclear and Fluid Mechanics, University of the Basque Country (UPV/EHU), Nieves Cano, 12, 01006 Vitoria-Gasteiz, Spain; aballesteros013@ikasle.ehu.eus (A.B.-C.); inigo.aramendia@ehu.eus (I.A.)

² Automatic Control and System Engineering Department, University of the Basque Country UPV/EHU, Nieves Cano 12, 01006 Vitoria-Gasteiz, Spain; ekaitz.zulueta@ehu.eus (E.Z.); jm.lopez@ehu.es (J.M.L.-G.)

* Correspondence: unai.fernandez@ehu.eus

Received: 12 June 2020; Accepted: 15 July 2020; Published: 19 July 2020



Abstract: Over the last few years, the advances in size and weight for wind turbines have led to the development of flow control devices. The current work presents an innovative method to model flow control devices based on a cell-set model, such as Gurney flaps (GFs). This model reuses the cells which are around the required geometry and a wall boundary condition is assigned to the generated region. Numerical simulations based on RANS equations and with $Re = 2 \times 10^6$ have been performed. Firstly, a performance study of the cell-set model on GFs was carried out by comparing it with a fully mesh model of a DU91W250 airfoil. A global relative error of 1.13% was calculated. Secondly, optimum GF lengths were determined (from 0% to 2% of c) for a DU97W300 airfoil and an application of them. The results showed that for lower angles of attack (AoAs) larger GFs were needed, and as the AoA increased, the optimum GF length value decreased. For the purpose of studying the effects generated by two flow control devices (vortex generators (VGs) and optimum GF) working together, a triangular VG based on the jBAY model was implemented. Resulting data indicated, as expected, that when both flow control devices were implemented, higher C_L and lower C_D values appeared.

Keywords: flow control; wind turbine; aerodynamics; Gurney flap; vortex generators

1. Introduction

The optimization of wind turbines is an engaging field of research for both academics and industrial parties within the renewable energy business. Recent studies by Chaviaropoulos [1], present the critical effect of power performance, especially for offshore projects. Consequently, as wind turbines get larger in diameter, apart from the economic benefit of performance enhancement, the blade's aerodynamic loads are increasing. Pechlivanoglou [2,3] and its reduction is also of interest. Miller [4] performed studies on the implementation of vortex generators (VGs) on a 2.5 MW HAWT and reported a maximum increase of 15.2% in the power output. Consequently, both passive and active flow control solutions are being considered and implemented thoroughly [5]. Passive flow control devices are those ones which do not need any external energy input, whereas active ones require external energy inputs to work [6].

Vortex generators (VGs) are plates mounted near the leading edge of airfoil. Their main purpose is to transfer high amounts of momentum near the surface and adjacent fluid layer, making the flow more resistant to the pressure adverse gradient, thereby mitigating the boundary layer separation [7]. Vortex generators are small vanes, usually triangular or rectangular, placed in the airfoil suction side. They are typically displayed in pairs [8,9] and with an angle of inclination with the inflow. Thanks to

these elements, the energy from the outer flow of the boundary layer (higher velocity) is transferred into the boundary layer inner region [10].

Navier–Stokes equations can be used to simulate the resulting lift force from a vane-type vortex generator in the flow field, but they require additional computational uncertainty and processing times; see Bender et al [11]. The physical effects of wake downstream vortex generators in a negligible streamwise pressure gradient flow were reproduced by Fernandez-Gamiz et al. [12] and Chillon et al. [13] by means of numerical simulations.

As the studies from above confirm the beneficial implementation of VGs to increase aerodynamic performance, Fernandez-Gamiz et al. [14] has reported the results for computational fluid dynamics (CFD) simulations for sub-boundary VGs with varying geometrical height. Additionally, another study from Fernandez-Gamiz et al. [12] reports the self-similarity and helical symmetry of the vortices' trail downstream after the vane.

Gurney flaps (GFs) are L-shaped permanent flaps located on the pressure side of the trailing edge of airfoils; see Kumar [15]. They got their name after US race-car driver Dan Gurney, who, in the early 1970s documented their aerodynamics effects.

The study of Gurney flaps' implementation and performance has been widely reported, both experimentally and numerically. According to Alber et al. [16], who analyzed wind tunnel tests for GFs on nine different airfoils and for different GF heights, GFs' effect on the C_L/C_D ratio is likely to be favorable as long as small heights are assumed. Moreover, they presented the effect on rotor blades computationally; the results suggest an enhanced power performance between 0.8% and 2.0% for small GF heights. It has been found that the lift coefficient enhancement is due to the simultaneous effects of the flow structure over the airfoil's trailing edge. In contrast with the sharp edge, its separation bubbles are substituted for two new thinner vortices by inducing lower drag, but the upstream separation bubble will increase it. Nevertheless, the whole aft-loading of the trailing edge region will increase such that the airflow is pushed downwards; therefore, the boundary layer separation is delayed over the suction side.

Fernandez-Gamiz et al. [17] reported CFD simulations on a S810 airfoil using Reynold's averaged Navier–Stokes (RANS) equations and the utilization of proper orthogonal decomposition for the CFD data aiming to build a reduced order method. The findings suggest that the implementation of proper orthogonal decomposition (POD) may be able to deliver numerical results at low computational cost.

The principal goal of the present work is the implementation of a Gurney Flap based on the cell-set model, on the DU97W300 airfoil. Jonkman et al. [18] presents a widely stated 5 MW wind turbine which was developed by NREL, where the DU97W300 airfoil is a component of the turbine. The major benefit of the cell-set model is its simple and straightforward implementation contrasted with the re-meshing process for a fully mesh model. Furthermore, this model provides flexibility in terms of geometrical and dimensional modifications. With the aim of validating the effectiveness of the cell-set model, a comparison with a fully mesh model has been carried out. VG and GF combinations were studied by means of the airfoil's lift-to-drag ratio (C_L/C_D), commonly known as the aerodynamic performance of the airfoil. The resulting data of the current work show precise error values for the validation process for the cell-set model and the application of optimum GF Length calculations.

The layout of this manuscript is organized in the following way: first, the applied CFD methodology is presented. In the subsequent section, different results are shown regarding to the simulation setups. Eventually, the last section provides essential and leading conclusions gathered from this study.

2. Materials and Methods

In this study, with the purpose of analyzing the performance of the cell-set model, two different airfoils were used: DU91W250 and DU97W300. These are typically used in multi-megawatt HAWT applications [18]. The performance of the cell-set model has been studied through the CFD commercial code STAR CCM+v14.02.012 [19].

2.1. Cell-Set Model

The model in which all the simulations were founded is based on leveraging the already generated mesh for the corresponding airfoil by using the cells wherein the matching geometry would be located. In other words, the required geometry has to be defined, and after that, the cells which are around the geometry are selected. The IDs of those cells are used to generate a new cell-set region and a wall boundary is assigned to that region. The application of this novel model on a GF has been the principal point of this study and it is considered that this has been the first implementation of the cell-set model. Figure 1 illustrates a sketch of the construction of a cell-set based on the geometry of a GF, for the two-dimensional case on the DU91W250 and for the three-dimensional case on the DU97W300.

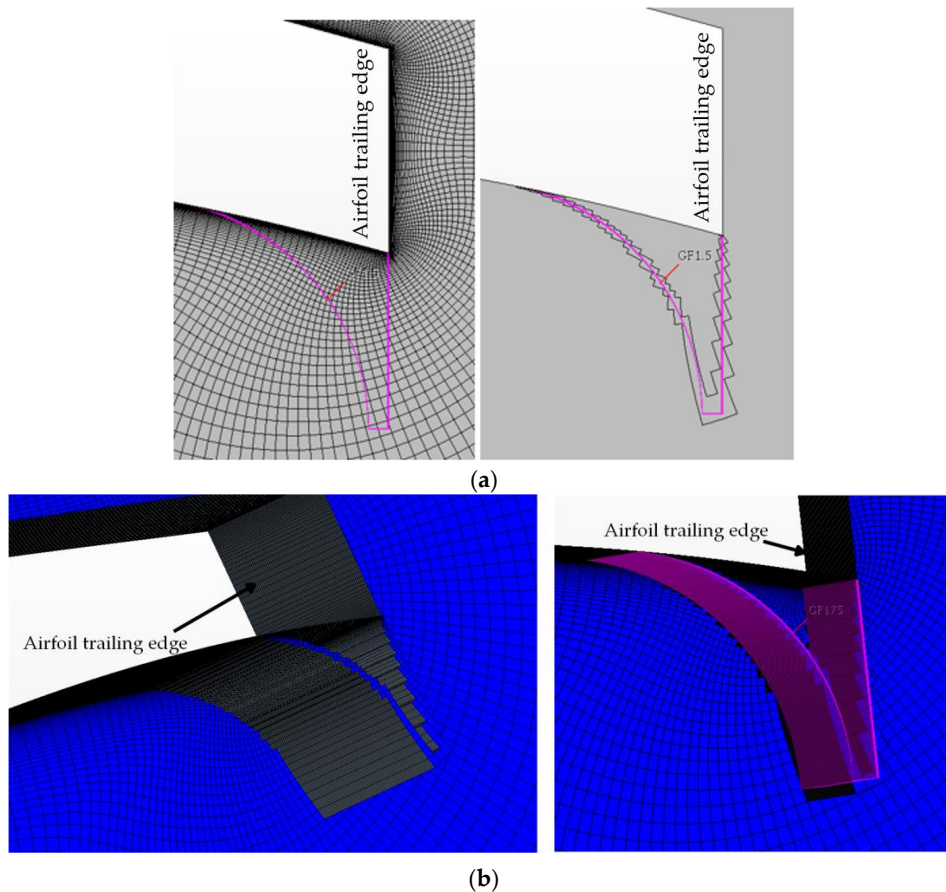


Figure 1. Cell-set construction based on the geometry of a GF: (a) two-dimensional case of a DU91W250 airfoil, equipped with a Gurney flap (GF) cell-set; (b) three-dimensional case of a DU97W300 airfoil, equipped with a GF cell-set (see Figure 3 for an entire airfoil context).

2.2. Numerical Setup

All the cases were performed with a Reynolds number of $Re = 2 \times 10^6$, based on each airfoil chord length. RANS equations were used to perform the numerical simulations. In particular, for these scenarios, the shear stress turbulence model SST studied by Menter [20] was chosen, wherein a union of the properties of the K-epsilon and K-omega models was accomplished. For the pressure-velocity coupling, the upwind algorithm was employed and the discretization of the mesh was performed by a linear upwind second order scheme.

The dynamic viscosity of the air was set at $\mu = 1.855 \times 10^{-5}$ Pa·s and kinematic viscosity at $\nu = 1.51 \times 10^{-5}$ m²/s. An air density value of $\rho = 1.204$ kg/m³ was introduced.

An O-meshed computational domain was determined for all the numerical simulations. As reported by Sørensen et al. [21], we recommend to set the mesh radius to 42 times the length of

the airfoil chord. The chord length of the DU91W250 is $c = 1$ m, whereas the chord length of the DU97W300(2D) has a value of $c = 0.65$ m. The grid domain of the DU91W250(2D) was composed of 65,348 finite elements; the first cell height was defined as $\Delta z/c$ of 1.351×10^{-6} , by means of its normalization with the airfoil chord. Therefore, a maximum skewness angle of 39.4° was formed. For the two-dimensional case of the DU97W300, the grid domain was composed of 105,472 finite parts. This instance, the first cell height was defined as $\Delta z/c$ of 7.915×10^{-6} and a maximum skewness angle of 35.78° was generated. Both airfoils had their surface boundary type set as a non-slip boundary. Enlarged views of these meshes are represented in Figure 2.

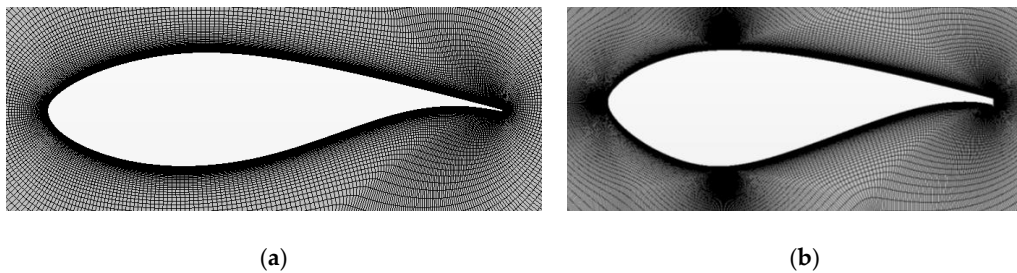


Figure 2. Enlarged views of the two-dimensional meshes on the airfoils: (a) DU91W250 airfoil; (b) DU97W300 airfoil.

2.2.1. Setup for Cell-Set Validation (2D)

Initially, a two-dimensional mesh of the DU91W250 was used in order to verify the performance of the cell-set model. For the GF lengths, a range between 0.25% and 2% for the chord length with a step of 0.25% for each GF length was defined. The AoAs were taken from 0° to 5° with a resolution of 1° among each simulation and the free stream velocity corresponds to $U_\infty = 30$ m/s. These ranges are based on the parametric study carried out by Aramendia et al. [22]. Results from that study show that for AoAs higher than 5° , the implementation of a GF is detrimental. All in all, a total of 48 different scenarios for this airfoil have been studied, according to the previously defined data.

2.2.2. Setup for Optimum GF Length Calculation (2D)

On the other hand, in order to determine which is the optimum GF length for each AoA, a two-dimensional mesh of the DU97W300 was used. The range of the GF lengths was also taken from 0.25% to 2% with a step of 0.25%. Nevertheless, for these cases the AoAs reached a wider span: from 0° to 20.24° according to the experimental data from Timmer [23]. A free stream velocity value of $U_\infty = 46.1142$ m/s was introduced. Two different flow states were chosen: at AoAs below 15.25° , the simulations were run in steady state, while for higher values an implicit unsteady physic was introduced. Consequently, as means to reach the optimum GF length values, the summing of 96 two-dimensional numerical solutions was performed.

2.2.3. Setup for Optimum GF Combined with a VG (3D)

Once the optimum GF lengths were defined, as a means to contrast the effects of the implementation of these ones, a VG was added in the suction side (at 30% of the chord length) of a clean DU97W300 so the results could be compared to the ones obtained by Timmer [23] and Gao et al. [24]; see Figure 3. The VG implementation has been performed by using the jBAY model presented in Chillon et al. [13]. A height of 5 mm and a length of 17 mm were defined for the triangular VG with an incidence angle of 18° to the oncoming flow. The principal variation for these cases is that a volume mesh is being used, instead of the surface mesh used in the two-dimensional cases. Hence, a three-dimensional work space is presented and the grid domain grows to 6,644,736 finite elements. The maximum skewness angle reached a value of 49.78° . In that instance, the computational domain was also O-shaped, but the radius was reduced to 30 times the chord. Symmetrical boundary planes were defined for the

lateral walls, and as in the previous cases, non-slip boundaries were applied to the airfoil. A farfield free stream state was assigned to the O-wall. The regions close to the trailing and leading edge of the airfoil, along with the VG area, were refined with a 1.1 growth-rate.

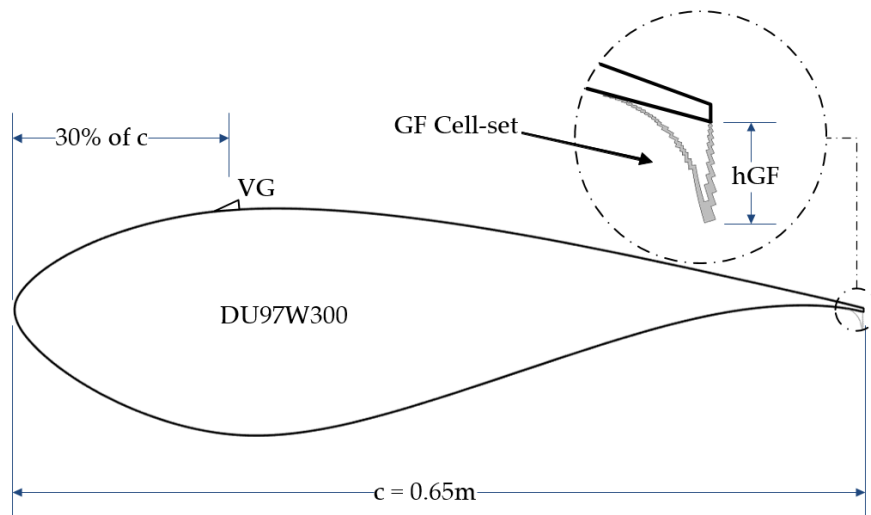


Figure 3. Sketch of the vortex generator (VG) (jBAY) and the GF (cell-set) setup. Chord value of $c = 0.65$ m, VG location at 30% of the chord length, and GF cell-set profile representation.

2.3. jBAY Model

In the present study, the jBAY source-term model introduced in Jirasek [25] and founded on the BAY model formulated by Bender et al. [11] has been used to model the effects of a VG. According to this method, a normal force is applied perpendicularly to the local flow direction; see Figure 4. The application of this force reproduces the forces generated by a VG, despite that there is not a meshed geometry of the VG. Lift forces are calculated for each cell of the VG region by Equation (1).

$$\vec{L}_{\text{cell}} = C_{\text{VG}} \cdot \rho (\vec{u} \cdot \vec{b}) (\vec{u} \cdot \vec{n}) \frac{\vec{u} \cdot \vec{t}}{\|\vec{u}\|} S_{\text{VG}} \frac{V_{\text{cell}}}{V_{\text{S}}} \quad (1)$$

where \vec{L}_{cell} is the lift force value for one element; C_{VG} is the relaxation factor which generally has a value around 10, according to Jirasek [25]. The density is defined as ρ , \vec{u} is the local velocity, and \vec{b} is a unit factor identified as $\vec{b} = \vec{n} \times \vec{t}$ (see vectors represented in Figure 4). The VG surface-area is determined as S_{VG} , V_{cell} is the volume of a one finite element, and V_{S} represents the total volume of the cell region; see Fernandez-Gamiz et al. [26] and Errasti et al. [27]. Equation (1) is introduced as a source-term field function and it is assigned as the momentum source of the VG region.

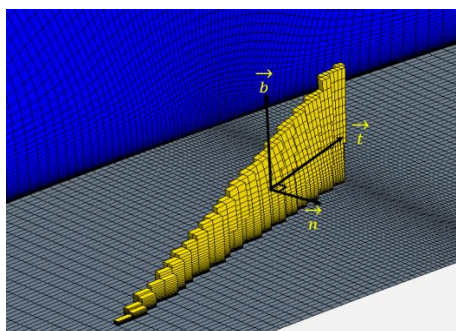


Figure 4. Cell-made representation of the triangular VG with the jBAY source-term model.

3. Results

Two key aspects are discussed in this section. On the one hand, the performance analysis of the cell-set model on a GF implementation was the first step to verify the effectiveness of the cell-set model. On the other hand, the selection of the optimum GF length for each AoA was carried out as an actual application of the cell-set model.

3.1. Cell-Set Performance

To evaluate the performance of the model, the mesh and results for the DU91W250 presented in Aramendia et al. [22] are the basis of this section. Hence, the results obtained with the cell-set model can be contrasted with the ones obtained with the fully mesh model. This has been studied by using the C_L/C_D lift-to-drag ratio as a function of the GF length for six AoAs, from 0° to 5° . Figure 5 represents for each AoA two different values: firstly, the C_L/C_D values for each hGF obtained from a fully mesh (FM) model, and secondly, the same parameters but based on the cell-set model. The horizontal black-dotted lines represent the C_L/C_D ratio of a clean profile (without flow control devices) for each AoA.

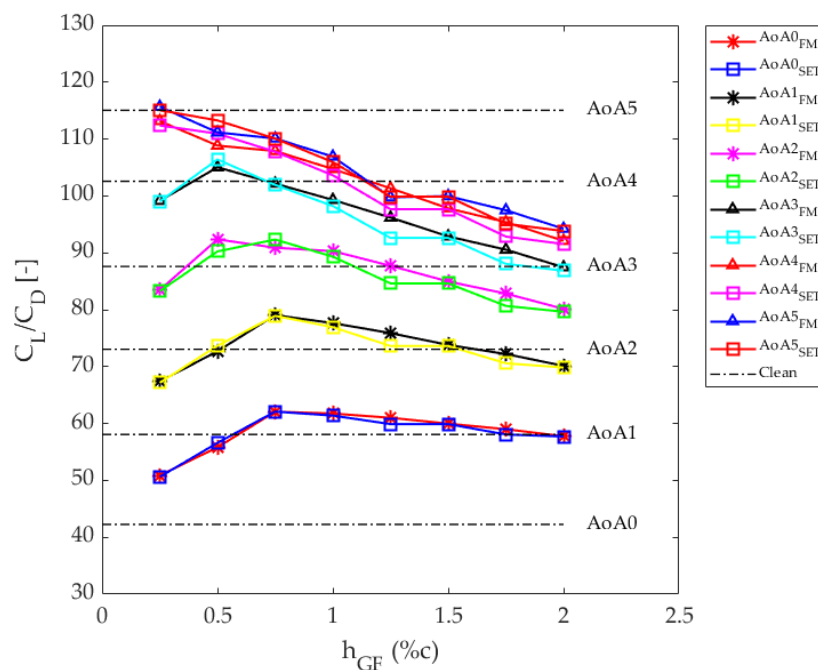


Figure 5. Lift-to-drag ratio (C_L/C_D) along the GF lengths for angles of attack (AoAs) from 0° to 5° . Quantitative comparison of the C_L/C_D ratio among the clean airfoil, fully mesh (FM) model and cell-set (SET) model. Square markers have been used to represent the cell-set curves.

In Figure 5 it is represented how from the AoAs 0° to 3° , both the cell-set and fully mesh values are on the upper part of the clean line. However, for 4° and 5° , the curves cross the clean line. Specifically, for 4° of AoA, the lift-to-drag ratio is solely improved for hGF below 1% of chord length. In this case a GF larger than 1% of the chord length produces a reduction in the growth of the C_L/C_D value. Consequently, the aerodynamic performance will be increased for angles below 3° .

As the evidence suggests, the cell-set curves follow the pattern of the fully mesh ones. Consequently, in order to measure the performance of the cell-set model, the relative error of each case has been calculated (see Table 1) by using the Equation (2). The “min” and “max” parameters refer to the minimum and maximum C_L/C_D values between the fully mesh and the cell-set model. After that, Equation (3) was used to determine the average error value of each cell-set GF case. As a result, a

global error of 1.13% was calculated, with the purpose of reaching a mean representative value for the error of the cell-set model; see Equation (4). The maximum error is 3.715% at 3° and 1.25% c.

$$e_{r_i} = \left(1 - \frac{\min\left(\frac{C_{L_i}}{C_{D_i}}\right)}{\max\left(\frac{C_{L_i}}{C_{D_i}}\right)} \right) \cdot 100 \quad (2)$$

$$e_{avg_j} = \frac{\sum_{i=1}^{N=6} e_{r_i}}{N} \quad (3)$$

$$e_g = \frac{\sum_{j=1}^{N=8} e_{avg_j}}{N} \quad (4)$$

Table 1. Relative error (%) for each case. The last row shows average errors for each hGF.

AoA [°]	hGF (% of c)							
	0.25	0.5	0.75	1	1.25	1.5	1.75	2
0	0.478	1.391	0.031	0.581	1.816	0.134	1.566	0.082
1	0.325	1.310	0.159	0.913	2.990	0.253	2.248	0.422
2	0.224	2.295	1.561	1.082	3.520	0.392	2.618	0.629
3	0.120	1.293	0.216	1.082	3.715	0.295	2.753	0.687
4	0.680	1.885	0.106	1.053	3.635	0.166	2.664	0.612
5	0.527	1.855	0.016	0.890	0.118	0.095	2.425	0.429
e_{avg_j} [%]	0.392	1.672	0.348	0.933	2.632	0.222	2.379	0.477

3.2. Calculation of the Optimum GF Lengths

As previously mentioned, the second part of this study consists of performing an actual application of the cell-set model. Specifically, the C_L/C_D ratio was calculated from 0° to 20.24° of AoA on the DU97W300 airfoil by means of two-dimensional numerical simulations.

Firstly, C_L lift coefficient and C_D drag coefficient curves were determined, as is shown in Figure 6. Both plots represent nine different curves in which the dashed-blue line shows the curve formed by a clean airfoil and the eight remaining continuous curves refer to the C_L and C_D values obtained with each GF length (% of c). A noticeable pattern is created: longer GFs generate higher C_L and C_D , whereas shorter GFs reach lower values.

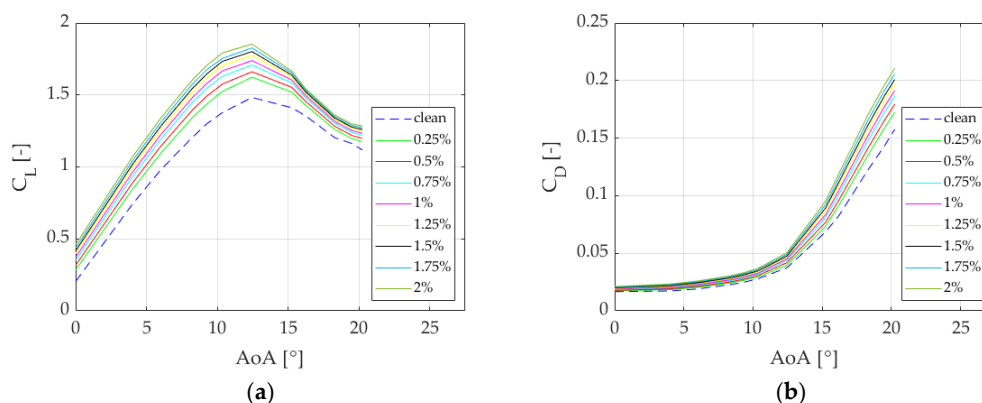


Figure 6. C_L (a) and C_D (b) curves of the DU97W300 airfoil with different GF lengths (0% to 2% of c).

Secondly, in order to understand the behavior of the profile, the aerodynamic performance variations (C_L/C_D lift-to-drag ratio variations) for each GF have been analyzed. Figure 7 describes two lines per AoA: black lines represent the C_L/C_D value of a clean airfoil (neither GF nor VG are

implemented) for the corresponding AoA, while the triangular-dotted blue curves show the value of the C_L/C_D ratio for each GF length from 0.25% to 2% of the chord length. Table 2 has been introduced to present the calculated C_L/C_D values of each simulation. The clean value is constant for each AoA, since there is no flow control device implemented. Nevertheless, those constant clean values have been taken as reference values to compare them to the values obtained with the cell-set GFs.

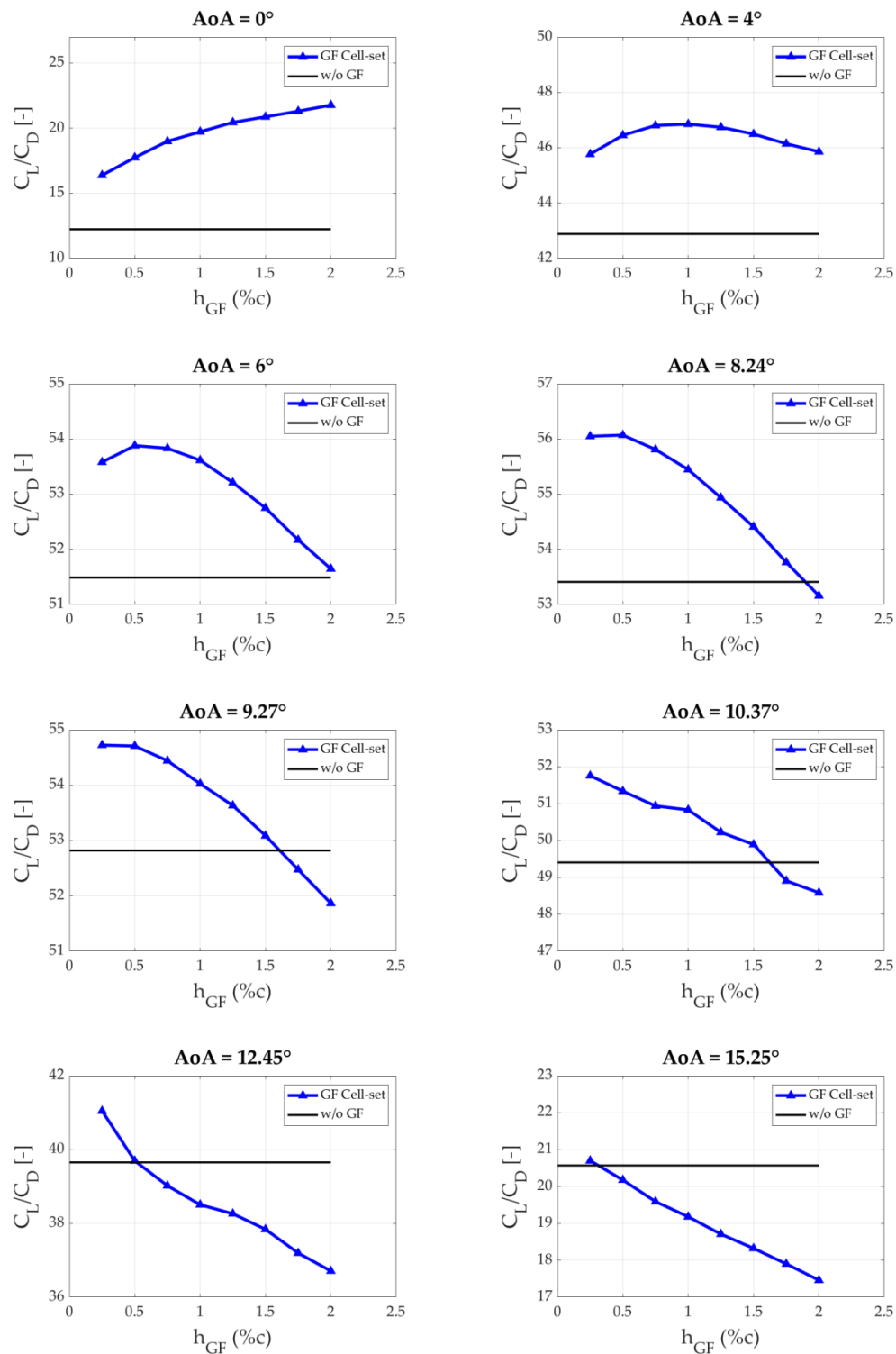


Figure 7. Cont.

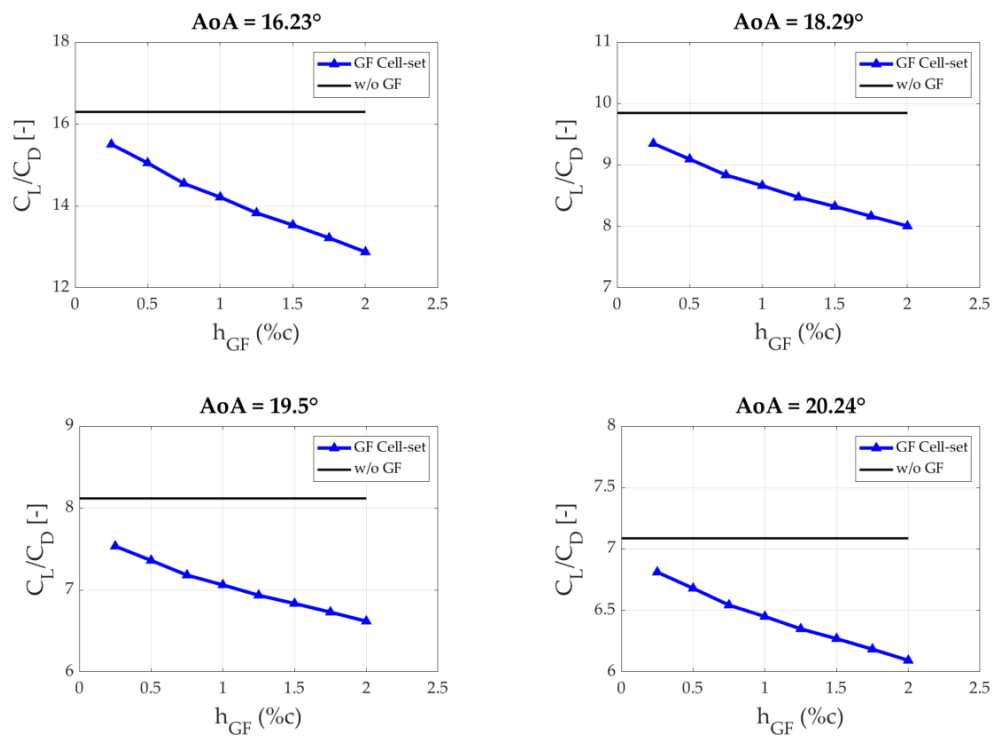


Figure 7. C_L/C_D lift-to-drag ratio from 0° to 20.24° of AoA on the DU97W300 airfoil. Two curves per AoA are represented: black curves represent the C_L/C_D values of a clean airfoil (no flow control devices) and the triangular-dotted blue curves show the values of the C_L/C_D ratio for each GF length from 0.25% to 2% of the chord length.

Table 2. C_L/C_D lift-to-drag ratio values for the GF implementation on the DU97W300 airfoil.

AoA [$^\circ$]	hGF (% of c)								
	No GF	0.25	0.5	0.75	1	1.25	1.5	1.75	2
0	12.24	16.39	17.75	18.99	19.73	20.45	20.87	21.31	21.77
4	42.89	45.77	46.45	46.80	46.85	46.74	46.49	46.14	45.86
6	51.49	53.58	53.88	53.83	53.61	53.21	52.75	52.17	51.65
8.24	53.41	56.05	56.07	55.81	55.45	54.93	54.41	53.77	53.16
9.27	52.82	54.70	54.71	54.44	54.02	53.63	53.09	52.47	51.86
10.37	49.41	51.75	51.34	50.94	50.83	50.22	49.89	48.91	48.58
12.45	39.65	41.05	39.69	39.02	38.50	38.26	37.84	37.19	36.71
15.25	20.57	20.70	20.17	19.59	19.18	18.71	18.32	17.90	17.46
16.23	16.30	15.50	15.05	14.55	14.21	13.83	13.53	13.22	12.88
18.29	9.85	9.35	9.09	8.84	8.66	8.47	8.33	8.17	8.01
19.5	8.12	7.53	7.36	7.18	7.06	6.93	6.83	6.73	6.62
20.24	7.09	6.81	6.68	6.54	6.45	6.35	6.27	6.18	6.09

It is clearly represented how the curves evolve along with the AoAs. When the AoA is set at 0° , the aerodynamic performance is increased due to the GF implementation in the whole GF length range. Additionally, at AoA = 0° , longer GFs provide a higher C_L/C_D value. In contrast, when the AoA value is increased, a descending tendency is illustrated on the evolution of the curves. This trend was also observed on the study presented by Aramendia et al. [22] for a DU91W250 airfoil. At 8.24° and 0.5% of hGF a maximum peak value of $C_L/C_D = 56.069$ was reached. For higher AoAs, the curves descend to the point that at 16.23° the implementation of a GF only produces a loss in the aerodynamic performance. Considering that 15.25° was the last studied angle in which the GF implementation improves the performance of the airfoil, it can be concluded that from 16.23° to 20.24° of AoA, any GF length of the studied range cannot supply a higher C_L/C_D ratio than the clean airfoil.

Taking into consideration the curves illustrated in Figure 7, a selection of the optimum GF length for each AoA was carried out. In order to perform the selection, the following criteria were applied: as long as the cell-set curve (blue curve with triangular markers), or a section of it, is on the upper part of the clean line, the maximum calculated value is chosen. Nevertheless, the cases in which the whole cell-set curve is below the clean line (from 16.23° to 20.24° of AoA) are rejected as there is no aerodynamic improvement. In Table 3, the optimum hGF values for each AoA and the C_L/C_D ratio reached are presented. Additionally, when AoA is close to 0°, longer GFs are requested, and as the AoA increases, lower hGF values are requested in order to achieve the maximum C_L/C_D ratio.

Table 3. Optimum GF lengths for each angle of attack.

AoA [°]	max. C_L/C_D [-]	Opt. hGF (% of c)
0	21.77	2
4	46.85	1
6	53.88	0.5
8.24	56.07	0.5
9.27	54.71	0.5
10.37	51.75	0.25
12.45	41.05	0.25
15.25	20.70	0.25

3.3. Application of the Optimum GFs

With the aim of studying the performances of the optimum GF lengths on the DU97W300 airfoil, a comparison with experimental data from a study made by Timmer et al. [23] and CFD results from Gao et al. [24] was carried out. In Figure 8, five curves per plot are represented: a green curve with cross markers illustrates the C_L and C_D values obtained by means of three-dimensional simulations in which VG (jBAY) and GF (cell-set) flow control devices have been implemented. The red curve with cross markers shows the C_L and C_D values reached in two-dimensional scenarios wherein the optimum GFs have been applied. Black curve with cross markers and the curve formed by blue crosses represent the results taken from [24] and [23] respectively, where a VG (with same position and dimensions) has been implemented. The continuous black curve shows the C_L and C_D values for a DU97W300 airfoil without flow control devices.

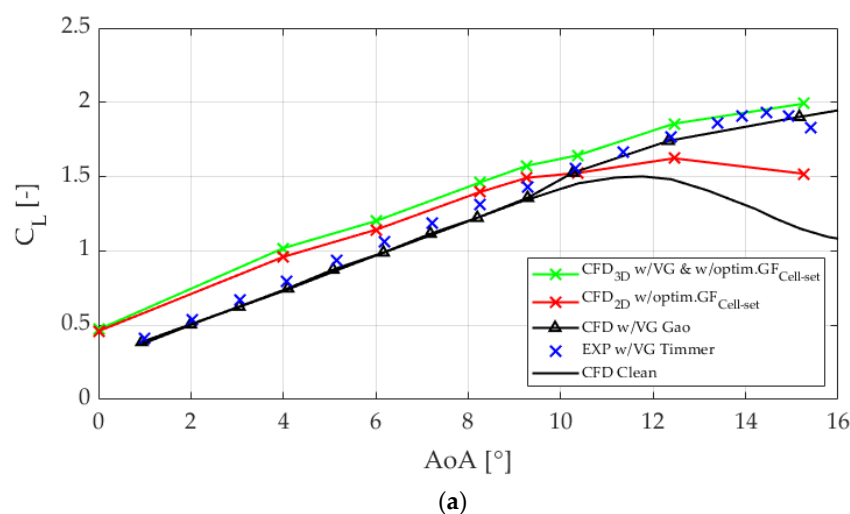


Figure 8. Cont.

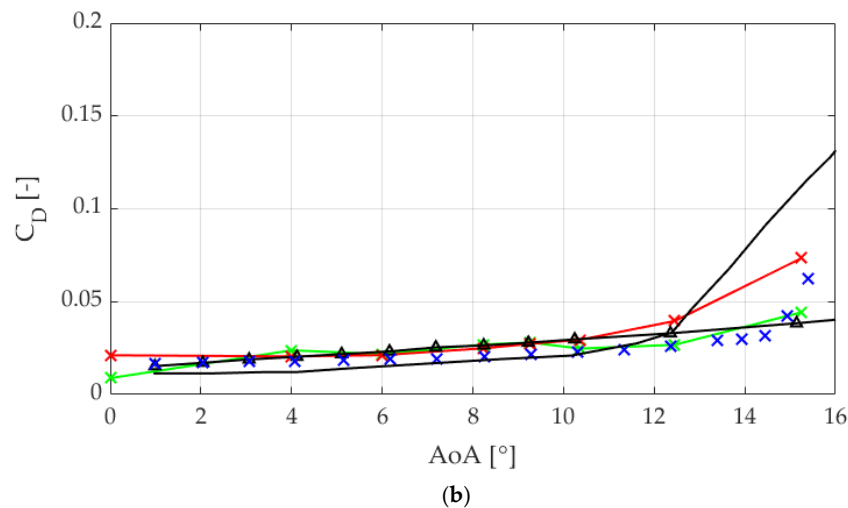


Figure 8. Representation of the influences of flow control devices on the (a) C_L and (b) C_D coefficient curves for the DU97W300 airfoil.

The results of C_L coefficients show a noticeable distinction among the curves. Firstly, the clean airfoil curve shows its maximum peak before arriving to 12.45° of AoA. However, when the DU97W300 has a VG on its suction side, the C_L curve remains growing, as it is the principal effect of a VG implementation [28,29]. On the other hand, if the optimum GF length is applied for each AoA, higher C_L values are reached for angles close to 0° . Furthermore, once the AoA goes further 12.45° , the GF keeps the curve higher than the clean one, not as much as the VG does though. All things considered, the implementation of both flow control devices (VG and optimum GF) at the same time generates the highest C_L curve in the whole AoA range; see the green curve of Figure 8a. Figure A1 of Appendix A represents the results regarding the pressure coefficient (C_p) of the clean airfoil in comparison with the flow-controlled airfoil. As previously determined, this flow-controlled case is defined as the airfoil with the triangular VG and the optimum GF for each AoA. As expected, slight differences are visible at low AoAs between the clean airfoil and the flow-controlled one. However, at higher AoAs an increase on the pressure coefficient is achieved due to the implementation of the flow control devices (VG and optimum GF). These results are in accordance with the values shown in Figure 8a since there is a direct relation between C_L and C_p . A small discontinuity is observed in the case of the flow-controlled airfoil due to the presence of the VG at the position of 30% of the chord length from the leading edge.

Another essential point is the effect of flow control devices on C_D coefficients. From 0° to 12.45° there is a minimal variation among the C_D curves. Despite this, after 12.45° the profiles with a VG present lower values than the clean and the GF airfoils.

4. Conclusions

In the present work, the performances of the cell-set model on two different airfoils (DU91W250 and DU97W300) were researched. This model reuses the cells of a mesh to generate new geometries, providing that the location of the cell-set is on a refined part of the mesh. Hence, an approach to the real dimensions of a geometry can be reproduced. This is a very flexible model, since the geometry can be modified without having to remesh the computational domain.

Firstly, to determine the performance of the cell-set model, two-dimensional simulations on a DU91W250 were performed by means of CFD. A comparison between the cell-set model and a fully mesh model was carried out. RANS equations were used at a Reynolds number of $Re = 2 \times 10^6$. The length of the GFs varies from 0% to 2% of the airfoil chord length (c) at AoAs from 0° to 5° . The results obtained showed that the maximum relative error value was of 3.715% and a global relative error (e_g) of 1.13% was calculated. Consequently, it is considered that the cell-set model is accurate enough to implement it in other scenarios.

Secondly, the DU97W300 airfoil was used with the aim of obtaining the optimum GF length (hGF) for each AoA. As in the previous case, hGFs were set from 0% to 2% of c . Nevertheless, a broader AoA range was established: from 0° to 20.24° . According to the numerical results, for lower AoAs, larger GF are needed to reach the maximum lift-to-drag ratio. As the AoA increases, the optimum hGF value decreases. This means that a fixed GF would not reach the optimum aerodynamic performance for the whole range of angles-of-attack. Subsequently, an active GF with variable length would be desirable. At 8.24° of AoA and 0.5% of hGF a maximum peak value of $C_L/C_D = 56.069$ was reached, and 15.25° was the last studied angle in which the GF implementation improved the performance of the airfoil. Thus, for the remaining AoAs, a GF implementation did not optimize the lift-to-drag ratio.

Finally, three-dimensional simulations were carried out. A triangular VG (based on the jBAY source-term model) was introduced on the suction side of a DU97W300 airfoil. At the same time, optimum GFs were implemented on the trailing edge for AoAs from 0° to 15.25° . A comparison between CFD and experimental data was carried out. As expected, when both flow control devices (triangular VG and optimum GF) were implemented, higher C_L values and lower C_D values were reached. However, when the working conditions required lower AoA values, the effect of a GF was enhanced.

Further research in this field will be performed to study the 3D effects due to the implementation of the GF based on the cell-set model, and the results should be compared with those obtained by the 2D simulations presented in this study. Additionally, the effects of different levels of unsteadiness due to the incoming turbulence in the atmospheric boundary layer must be included in future studies of the implementation of the GF based on the cell-set model.

Author Contributions: A.B.-C., U.F.-G., and E.Z. formulated and carried out the numerical simulations; A.B.-C., U.F.-G., I.A., and J.M.L.-G. analyzed the resulting data and provided effectual guidelines for the manuscript preparation. All authors have read and agreed to the published version of the manuscript.

Funding: The authors are thankful to the government of the Basque Country and the University of the Basque Country UPV/EHU for the SAIOTEK (S-PE11UN112) and EHU12/26 research programs, respectively.

Acknowledgments: The authors are grateful for the support provided by SGIker of UPV/EHU. This research has been developed under the framework of the Joint Research Laboratory on Offshore Renewable Energy (JRL-ORE).

Conflicts of Interest: The authors declare no conflict of interest.

Nomenclature

	Definition
CFD	Computational fluid dynamics
GF	Gurney Flap
VG	Vortex generator
RANS	Reynolds-averaged Navier–Stokes
SST	Shear stress transport
ρ	Local density (kg/m^3)
μ	Dynamic viscosity ($\text{Pa}\cdot\text{s}$)
AoA	Angle of attack (deg)
c	Airfoil chord length (m)
hGF	Gurney flap length (% of c)
e_{r_i}	Relative error for each case (%)
e_{avg_j}	Average relative error for each hGF (%)
e_g	Global relative error (%)
C_D	Drag coefficient
C_L	Lift coefficient
C_P	Pressure coefficient
Re	Reynolds number
U_∞	Free stream velocity (m/s)
POD	Proper orthogonal decomposition

Appendix A

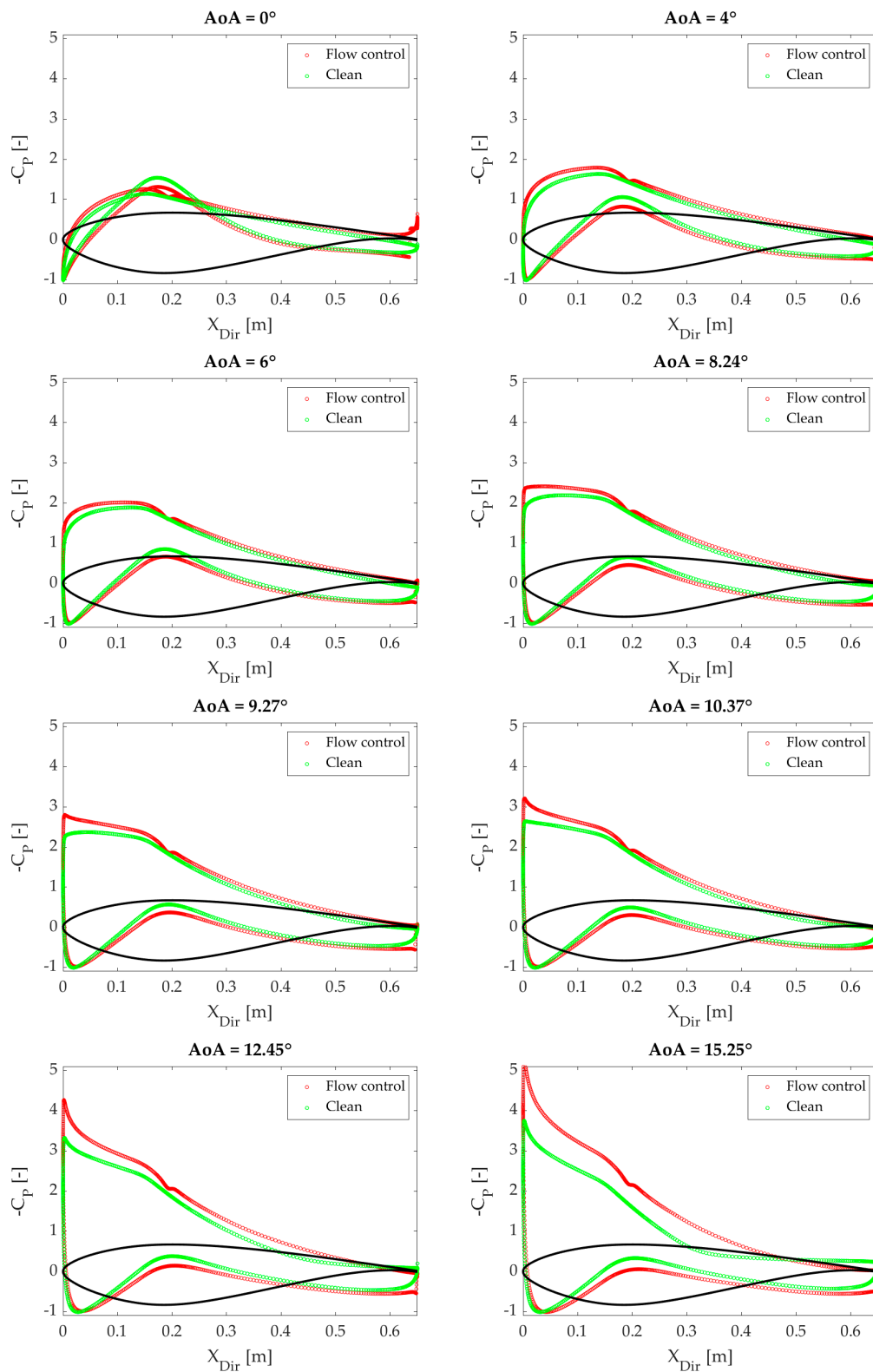


Figure A1. C_p pressure coefficient values from 0° to 15.25° of AoA on the DU97W300 airfoil. Green circles represent the values reached without flow control devices. Red circles show the pressure coefficients (C_p) for a DU97W300 airfoil with flow control devices (triangular VG and optimum GF).

References

1. Chaviaropoulos, P. Economic Aspects of Wind Turbine Aerodynamics. In *Handbook of Wind Energy Aerodynamics*; Springer Science and Business Media LLC: Berlin/Heidelberg, Germany, 2020; pp. 1–30.
2. Pechlivanoglou, G.; Nayeri, C.; Paschereit, C. Performance Optimization of Wind Turbine Rotors with Active Flow Control (Part 1). *Mech. Eng.* **2012**, *134*, 51. [[CrossRef](#)]
3. Pechlivanoglou, G.; Nayeri, C.; Paschereit, C. Performance Optimization of Wind Turbine Rotors with Active Flow Control (Part 2). *Mech. Eng.* **2012**, *134*, 55. [[CrossRef](#)]
4. Miller, G.E. *Comparative Performance Tests on the Mod-2, 2.5-mW Wind Turbine with and without Vortex Generators*; Boeing Aerospace Company: Seattle, WA, USA, 1995. Available online: <https://ntrs.nasa.gov/archive/nasa/casi.ntrs.nasa.gov/19950021557.pdf> (accessed on 3 February 2020).
5. Iradi, I.A.; Gamiz, U.F.; Saiz, J.S.; Guerrero, E.Z. State of The Art of Active and Passive Flow Control Devices for Wind Turbines. *DYNA Ing. E Ind.* **2016**, *91*, 512–516. [[CrossRef](#)]
6. Aramendia, I.; Fernandez-Gamiz, U.; Ramos-Hernanz, J.; Sancho, J.; Lopez-Guede, J.M.; Zulueta, E. Flow Control Devices for Wind Turbines. In *Lecture Notes in Energy*; Springer Science and Business Media LLC: Berlin/Heidelberg, Germany, 2017; Volume 37, pp. 629–655.
7. Hansen, M.O.L.; Madsen, H.A. Review Paper on Wind Turbine Aerodynamics. *J. Fluids Eng.* **2011**, *133*, 114001. [[CrossRef](#)]
8. Velte, C.; Hansen, M.O.L. Investigation of flow behind vortex generators by stereo particle image velocimetry on a thick airfoil near stall. *Wind. Energy* **2012**, *16*, 775–785. [[CrossRef](#)]
9. Godard, G.; Stanislas, M. Control of a decelerating boundary layer. Part 1: Optimization of passive vortex generators. *Aerosp. Sci. Technol.* **2006**, *10*, 181–191. [[CrossRef](#)]
10. Gutierrez-Amo, R.; Fernandez-Gamiz, U.; Errasti, I.; Zulueta, E. Computational Modelling of Three Different Sub-Boundary Layer Vortex Generators on a Flat Plate. *Energies* **2018**, *11*, 3107. [[CrossRef](#)]
11. Bender, E.E.; Anderson, B.H.; Yagle, P.J. Vortex Generator Modelling for Navier–Stokes Codes. In Proceedings of the 3rd ASMEJSME Fluids Engineering Conference, San Francisco, CA, USA, 18–23 July 1999.
12. Fernandez-Gamiz, U.; Velte, C.; Réthoré, P.-E.; Sørensen, N.N.; Egusquiza, E. Testing of self-similarity and helical symmetry in vortex generator flow simulations. *Wind. Energy* **2015**, *19*, 1043–1052. [[CrossRef](#)]
13. Chillón, S.; Uriarte-Uriarte, A.; Aramendia, I.; Martínez-Filgueira, P.; Fernandez-Gamiz, U.; Ibarra-Udaeta, I. jBAY Modeling of Vane-Type Vortex Generators and Study on Airfoil Aerodynamic Performance. *Energies* **2020**, *13*, 2423. [[CrossRef](#)]
14. Fernandez-Gamiz, U.; Errasti, I.; Gutierrez-Amo, R.; Boyano, A.; Barambones, O. Computational Modelling of Rectangular Sub-Boundary Layer Vortex Generators. *Appl. Sci.* **2018**, *8*, 138. [[CrossRef](#)]
15. Kumar, P.M.; Samad, A. Introducing Gurney flap to Wells turbine blade and performance analysis with OpenFOAM. *Ocean Eng.* **2019**, *187*, 106212. [[CrossRef](#)]
16. Alber, J.; Pechlivanoglou, G.; Paschereit, C.O.; Twele, J.; Weinzierl, G. Parametric Investigation of Gurney Flaps for the Use on Wind Turbine Blades. In *Proceedings of the Volume 1: Aircraft Engine; Fans and Blowers; Marine; Honors and Awards*; ASME International: Charlotte, NC, USA, 2017; Volume 9, p. 009-49-015.
17. Fernandez-Gamiz, U.; Mármol, M.M.G.; Rebollo, T.C. Computational Modeling of Gurney Flaps and Microtabs by POD Method. *Energies* **2018**, *11*, 2091. [[CrossRef](#)]
18. Jonkman, J.; Butterfield, S.; Musial, W.; Scott, G. *Definition of a 5-MW Reference Wind Turbine for Offshore System Development*; Technical Report NREL/TP-500-38060; National Renewable Energy Laboratory: Golden, CO, USA, 2009.
19. Siemens Star CCM+ Version 14.02.012. Available online: <https://www.plm.automation.siemens.com/global/en/> (accessed on 3 February 2020).
20. Menter, F.R. Two-equation eddy-viscosity turbulence models for engineering applications. *AIAA J.* **1994**, *32*, 1598–1605. [[CrossRef](#)]
21. Sieros, G.; Jost, E.; Lutz, T.; Papadakis, G.; Voutsinas, S.; Barakos, G.; Colonia, S.; Baldacchino, D.; Baptista, C.; Ferreira, C. CFD code comparison for 2D airfoil flows. *J. Physics Conf. Ser.* **2016**, *753*, 082019. [[CrossRef](#)]
22. Aramendia, I.; Fernandez-Gamiz, U.; Zulueta, E.; Saenz-Aguirre, A.; Teso-Fz-Betoño, D. Parametric Study of a Gurney Flap Implementation in a DU91W (2) 250 Airfoil. *Energies* **2019**, *12*, 294. [[CrossRef](#)]
23. Timmer, W.A.; van Rooij, R.P.J.O.M. Summary of the Delft University Wind Turbine Dedicated Airfoils. *J. Sol. Energy Eng.* **2003**, *125*, 488–496. [[CrossRef](#)]

24. Gao, L.; Zhang, H.; Liu, Y.; Han, S. Effects of vortex generators on a blunt trailing-edge airfoil for wind turbines. *Renew. Energy* **2015**, *76*, 303–311. [[CrossRef](#)]
25. Jirasek, A. Vortex-Generator Model and Its Application to Flow Control. *J. Aircr.* **2005**, *42*, 1486–1491. [[CrossRef](#)]
26. Fernandez, U.; Réthoré, P.-E.; Sørensen, N.N.; Velte, C.M.; Zahle, F.; Egusquiza, E. Comparison of four different models of vortex generators. In Proceedings of the EWEA 2012—European Wind Energy Conference & Exhibition, Copenhagen, Denmark, 16–19 March 2012.
27. Errasti, I.; Gamiz, U.F.; Martínez-Filgueira, P.; Blanco, J. Source Term Modelling of Vane-Type Vortex Generators under Adverse Pressure Gradient in OpenFOAM. *Energies* **2019**, *12*, 605. [[CrossRef](#)]
28. Zhao, Z.; Li, T.; Wang, T.; Liu, X.; Zheng, Y. Numerical investigation on wind turbine vortex generators employing transition models. *J. Renew. Sustain. Energy* **2015**, *7*, 063124. [[CrossRef](#)]
29. Li, X.; Liu, W.; Zhang, T.; Wang, P.; Wang, X. Analysis of the Effect of Vortex Generator Spacing on Boundary Layer Flow Separation Control. *Appl. Sci.* **2019**, *9*, 5495. [[CrossRef](#)]



© 2020 by the authors. Licensee MDPI, Basel, Switzerland. This article is an open access article distributed under the terms and conditions of the Creative Commons Attribution (CC BY) license (<http://creativecommons.org/licenses/by/4.0/>).